JOURNAL OF SOLID STATE CHEMISTRY **141,** 492–499 (1998)
ARTICLE NO. SC988001

Synthesis and Structural Study of Hexagonal Perovskites in the $Ba_5Ta_4O_{15}$–$MZrO_3$ (M = Ba, Sr) System

A. M. Abakumov, R. V. Shpanchenko, and E. V. Antipov

Department of Chemistry, Moscow State University, 119899 Moscow, Russia

and

O. I. Lebedev,[1] G. Van Tendeloo,[2] and S. Amelinckx

EMAT, University of Antwerp (RUCA), Groenenborgerlaan 171, B-2020 Antwerp, Belgium

Received June 8, 1998; accepted August 5, 1998

New cation-deficient perovskite-like oxides $Ba_5MTa_4ZrO_{18}$ and $Ba_5MTa_4Zr_2O_{21}$ (M = Ba, Sr) were synthesized and studied by X-ray diffraction, electron diffraction, and high-resolution electron microscopy (HREM). The $Ba_5SrTa_4ZrO_{18}$ (space group $R\bar{3}m$, ($hccch$), a = 5.80162(8) Å, c = 42.5403(8) Å, R_I = 0.039, R_p = 0.082) and $Ba_5Sr_2Ta_4ZrO_{21}$ (space group $R\bar{3}m$, $(hccccch)_3$, a = 5.7998(1) Å, c = 49.595(1) Å, R_I = 0.033, R_p = 0.080) crystal structures were refined from X-ray powder diffraction data. The results of structure refinements were confirmed by HREM observations. The formation of the $Ba_5Sr_3Ta_4Zr_3O_{24}$ compound was revealed and the structure of this compound was deduced from HREM (space group $P\bar{3}m1$, $hccccccch$, $a \approx 5.8$ Å, $c \approx 18.9$ Å). All these compounds belong to the $A_nB_{n-1}O_{3n}$ homologous series of cation-deficient hexagonal perovskite-like oxides with n = 6, 7, and 8 and may be formally described as intergrowth structures with alternating $Ba_5Ta_4O_{15}$-type and $Ba(Sr)ZrO_3$-type structural blocks along the c axis. © 1998 Academic Press

Key Words: **hexagonal perovskites; synthesis; X-ray powder diffraction; HREM.**

1. INTRODUCTION

The crystal structure of hexagonal perovskite-like oxides is usually considered as a sequence of close-packed AO_3 layers formed by large A cations (Ca, Sr, Ba, La) and oxygen atoms. One-third of the interstices in the close-packed framework are octahedrally coordinated exclusively by oxygen atoms and can be occupied by B cations, which often are highly charged transition metals. If the sum of the formal charges for A and B cations exceeds 6, the requirement of electroneutrality can be obeyed by the appearance of cation vacancies on the B sublattice. The B-cation deficiency can be accommodated as complete layers of empty octahedral interstices; a generalized description of the building principles for such cation-deficient hexagonal perovskite-like $A_nB_{n-\delta}O_{3n}$ oxides is given in (1). The presence of a *chhc* stacking fragment (h = hexagonal stacking, c = cubic stacking) results in a chain of three face-sharing octahedra (FSO), oriented along the hexagonal c axis. If the oxidation state of the B cations does not allow the formation of a metal–metal bond, the occupation of the middle octahedron in the *chhc* lamellae is unfavorable due to a strong electrostatic repulsion between B cations with a high formal charge. The stacking sequence for this fragment is described as $\begin{smallmatrix}A & \gamma B\\ c & h\end{smallmatrix}\ \square\ \begin{smallmatrix}A & \gamma B\\ h & c\end{smallmatrix}$, where is a $\square$ vacant B-cation layer and γ indicates a completely filled B-cation layer. The structure can then be described as consisting of blocks, separated by vacancy layers. It was shown in (1) that the $A_nB_{n-\delta}O_{3n}$ composition can be generated for any integer δ using not more than two different structural blocks having $A_mB_{m-1}O_{3m}$ and $A_{m+1}B_mO_{3(m+1)}$ compositions with abundancies p and q, respectively. The following relations were formulated to connect p and q with the phase composition:

$$m \le n/\delta < m + 1$$

$$p = (m + 1)\delta - n$$

$$q = n - m\delta.$$

The simplest case is realized for $\delta = 1$; then $n = m$, $p = 1$, $q = 0$, and the structure consists only of a single type of block of n AO_3 layers. For n = threefold or n = threefold + 1, the structures have rhombohedral symmetry, the stacking only repeats after three blocks, and n is the number

[1] On leave from the Institute of Crystallography RAS, Leninsky pr. 59, 117333 Moscow, Russia.

[2] To whom correspondence should be addressed.

0022-4596/98 $25.00

of layers per one-third of the c period. If n = threefold − 1, the repeat period along the c axis of the primitive trigonal lattice contains only one block. Compounds with such a structural organization belong to the $A_nB_{n-1}O_{3n}$ homologous series. The structure of any $A_nB_{n-1}O_{3n}$ homologue may also be deduced by insertion of additional AO_3 layers between the *chhc* lamellae. The crystal structure of $Ba_3Re_2O_9$ (2) should be considered as the first member of this series since it comprises the interconnected *chhc* lamellae only. According to this consideration, the final formulae $A_nB_{n-1}O_{3n}$ may be written as $A_3B_2O_9 + (n-3)ABO_3$ ($n \geq 3$). $A_nB_{n-1}O_{3n}$ homologues with close packings containing 5, 9, 12, 18, and 21 layers are known (1–6). For example, the insertion of close-packed layers of ABO_3 (A = Ca, La; B = Ti, Fe) perovskite into the $La_4Ti_3O_{12}$ matrix $(hcch)_3$ (7) is accompanied by the formation of two successive homologues $ALa_4Ti_3BO_{15}$ (*hccch*) and $A_2La_4Ti_3B_2O_{18}$ ($(hccch)_3$) (8–10). The resulting structures can be formally interpreted as an intergrowth between $La_4Ti_3O_{12}$ and the perovskite ABO_3 packing along the c axis.

Considering $Ba_5Ta_4O_{15}$ (5H *hccch*) (3) as the third member of the $A_nB_{n-1}O_{3n}$ homologous series, one can expect the existence of hexagonal perovskites with an ordered alternation of $Ba_5Ta_4O_{15}$ and ABO_3 blocks along the c axis. The aim of the present investigation is to study the preparation and structural aspects of the $A_nB_{n-1}O_{3n}$ homologues based on $Ba_5Ta_4O_{15}$ and $AZrO_3$ (A = Ba, Sr) blocks.

2. EXPERIMENTAL

All samples were prepared by the routine solid-state technique using $BaCO_3$, $SrCO_3$, Ta_2O_5, ZrO_2, and TiO_2 as initial reagents. Stoichiometric amounts of the starting materials were mixed in an agate mortar under acetone and pressed into pellets. The pellets were heated in a Nabertherm furnace at 1150°C for 20 h and at 1600°C for 60 h. The annealings were carried out in alumina crucibles in air. All samples were finally furnace cooled.

Phase composition and lattice parameters of the samples were determined using a focusing Guinier FR-552 camera (Cu$K\alpha_1$ radiation; germanium was used as an internal standard). Raw data for powder structure refinement were collected on a STADI-P diffractometer (Cu$K\alpha_1$ radiation curved Ge monochromator, transmission mode, step 0.02°(2θ), scintillation counter).

The RIETAN-97 (11) program was used for powder crystal structure refinement. The final refinement was carried out by the Rietveld method with a pseudo-Voigt profile function.

Electron diffraction (ED) and high-resolution electron microscopy (HREM) investigations were made on powdered samples deposited on holey carbon grids. The observations were performed using a JEOL 4000 EX microscope operating at 400 kV. The Scherzer resolution of the microscope is of the order of 1.7 Å. Image simulations were carried out with Mac Tempas software.

3. RESULTS

3.1. X-Ray Measurements

Both $Ba_5SrTa_4ZrO_{18}$ and $Ba_5Sr_2Ta_4Zr_2O_{21}$ were obtained as single-phase materials. However, we were unable to prepare $Ba_6Ta_4ZrO_{18}$ and $Ba_7Ta_4Zr_2O_{21}$ compounds in a pure form. The $Ba_6Ta_4ZrO_{18}$ compound always contains an admixture of $Ba_7Ta_4Zr_2O_{21}$, whereas the $Ba_7Ta_4Zr_2O_{21}$ compound was obtained only in a mixture with the $Ba_6Ta_4ZrO_{18}$ homologue. The X-ray diffraction patterns for all synthesized compounds were indexed on a hexagonal lattice with unit cell parameters listed in Table 1.

The crystal structures of $Ba_5SrTa_4ZrO_{18}$ and $Ba_5Sr_2Ta_4Zr_2O_{21}$ were refined from X-ray powder data. Since the reflections with $-h + k + l \neq 3n$ were systematically absent on the X-ray patterns of both compounds, the $R\bar{3}m$ space group was chosen. The starting positions of the heavy atoms and of the oxygen atoms were taken from the model of the $(hcccch)_3$ and $(hccccch)_3$ close packings, respectively. The refinements were carried out on the assumption that the occupancies of all A positions by Ba and Sr and B positions by Ta and Zr are equal. The thermal parameters for A and B cations were combined into two separate blocks to overcome the correlation effects and were refined in an isotropic approximation. Refined values of the thermal parameters for oxygen atoms were obtained to be close to zero, or even slightly negative. They were fixed to be equal to 1 Å^2 for the final refinement. This changed neither the values of the reliability factors nor the atomic coordinates. The influence of the preferred orientation along the [001] axis was taken into account by the Sasa–Uda function.

The parameters of the Rietveld refinement and reliability factors for both compounds are given in Table 2. Positional and thermal parameters and selected interatomic distances are listed in Tables 3 and 4 for $Ba_5SrTa_4ZrO_{18}$ and in Tables 5 and 6 for $Ba_5Sr_2Ta_4Zr_2O_{21}$. Experimental, calculated, and difference X-ray patterns are shown in Figs. 1a and 1b, respectively. The structure of both compounds are shown in Fig. 2.

TABLE 1
Unit Cell Parameters for $Ba_5MTa_4ZrO_{18}$ and $Ba_5M_2Ta_4Zr_2O_{21}$ (M = Ba, Sr) Compounds

Composition	a (Å)	c (Å)	Packing
$Ba_5SrTa_4ZrO_{18}$	5.8012(5)	42.535(2)	$(hcccch)_3$
$Ba_6Ta_4ZrO_{18}$	5.8166(2)	42.631(1)	$(hcccch)_3$
$Ba_5Sr_2Ta_4Zr_2O_{21}$	5.7999(9)	49.604(9)	$(hccccch)_3$
$Ba_7Ta_4Zr_2O_{21}$	5.8210(4)	50.063(3)	$(hccccch)_3$

TABLE 2
Parameters of Rietveld Refinement of $Ba_5SrTa_4ZrO_{18}$ and $Ba_5Sr_2Ta_4Zr_2O_{21}$ Crystal Structures

Compound	$Ba_5SrTa_4ZrO_{18}$	$Ba_5Sr_2Ta_4Zr_2O_{21}$
Space group	$R\bar{3}m$	$R\bar{3}m$
a (Å)	5.80162(8)	5.7998(1)
c (Å)	42.5403(8)	49.595(1)
Z	3	3
Cell volume (Å^3)	1240.02(3)	1444.76(5)
Calculated density (g/cm^3)	7.542	7.263
2θ range, step (deg)	$4 \le 2\theta \le 95$, 0.02	$5 \le 2\theta \le 100$, 0.02
Number of reflections	184	233
Refinable structural parameters	21	16
R_I, R_p, R_{wp}	0.039, 0.082, 0.114	0.033, 0.080, 0.107
Preferred orientation parameters		
p_1 and p_2 along [001] axis	127(5), 0.0011(2)	71(5), 0.0011(2)

3.2. Electron Diffraction

The electron diffraction patterns along the most relevant zone axes [0001]*, [11$\bar{2}$0]*, and [10$\bar{1}$0]* for $Ba_5SrTa_4ZrO_{18}$ and $Ba_5Sr_2Ta_4Zr_2O_{21}$ are reproduced in Fig. 3. Apart from a small difference in the cell parameters, the [0001]* patterns for both compounds are similar (Fig. 3a). The reflections are arranged in a hexagonal array corresponding to a lattice parameter $a = 5.8$ Å. The intensities of the spots can clearly be distributed in two categories; the brightest spots obey the extinction condition $-h + k = 3n$, imposed by the $R\bar{3}m$ space group. The less intense reflections appear to be due to diffraction from the first-order Laue zone (FOLZ), since the FOLZ are close enough to the Ewald's sphere to touch it by relrods from the $h0\bar{h}1$ and $h0\bar{h}\bar{1}$ reflections.

The [11$\bar{2}$0]* diffraction patterns exhibit a rhombohedral shift of the spot rows along c^* over $h \times \frac{1}{3}c^*$. In the [11$\bar{2}$0]* and [10$\bar{1}$0]* diffraction patterns, the most intense spots in the basal row (indicated by arrows) correspond to $l = 18$ for $Ba_5SrTa_4ZrO_{18}$ (Figs. 3b and 3c) and $l = 21$ for $Ba_5Sr_2Ta_4Zr_2O_{21}$ (Figs. 3d and 3e). The interplanar distance corresponding to these reflections is equal to the thickness of the Ba(Sr)O_3 layer. The spacing between spots in the rows corresponds to six Ba(Sr)O_3 layers for $Ba_5SrTa_4ZrO_{18}$ and seven Ba(Sr)O_3 layers for $Ba_5Sr_2Ta_4Zr_2O_{21}$, thus indicating the length of one-third of the repeat period of the rhombohedral cell along the c axis. The only diffraction condition $-h + k + l = 3n$ is deduced from the [11$\bar{2}$0]* and [10$\bar{1}$0]* diffraction patterns of both compounds.

TABLE 4
Selected Interatomic Distances for $Ba_5SrTa_4ZrO_{18}$ (Å)

BaSr(1)–O(1)	$2.77(2) \times 3$	BaSr(3)–O(3)	$2.903(1) \times 6$
BaSr(1)–O(2)	$2.911(2) \times 6$	BaSr(3)–O(3)	$3.03(3) \times 3$
BaSr(1)–O(3)	$2.97(3) \times 3$	TaZr(1)–O(3)	$2.10(3) \times 6$
BaSr(2)–O1)	$2.71(2) \times 3$	TaZr(2)–O(1)	$1.82(2) \times 3$
BaSr(2)–O(1)	$2.932(3) \times 6$	TaZr(2)–O(2)	$1.94(2) \times 3$
BaSr(2)–O(2)	$3.25(2) \times 3$	TaZr(3)–O(2)	$2.05(3) \times 3$
BaSr(3)–O(2)	$2.85(3) \times 6$	TaZr(3)–O(3)	$2.22(2) \times 3$

3.3. High-Resolution Electron Microscopy

3.3.1. Perfect structure. High-resolution images of $Ba_5SrTa_4ZrO_{18}$ and $Ba_5Sr_2Ta_4Zr_2O_{21}$ were obtained along the most informative [10$\bar{1}$0] zone (Figs. 4a and 4b). Along this zone the structure is viewed parallel to the columns of close-packed Ba(Sr)–O–Ba(Sr)–O rows; this directly reveals the stacking sequence. These columns are projected as rows of brighter dots. In the centers of parallelograms formed by the brightest dots, rows of less bright dots become visible in the thinnest part of the crystallite; they correspond to the projection of the Ta,Zr columns.

TABLE 3
Positional and Thermal Parameters for $Ba_5SrTa_4ZrO_{18}$

Atom	Position	x/a	y/b	z/c	B_{iso}(Å^2)
BaSr(1)[a]	6c	0	0	0.0888(2)	0.63(9)
BaSr(2)[a]	6c	0	0	0.1857(2)	0.63(9)
BaSr(3)[a]	6c	0	0	0.3613(2)	0.63(9)
TaZr(1)[b]	3a	0	0	0	1.24(9)
TaZr(2)[b]	6c	0	0	0.4488(1)	1.24(9)
TaZr(3)[b]	6c	0	0	0.2757(2)	1.24(9)
O(1)	18h	0.180(2)	$-x$	0.1382(6)	1.0
O(2)	18h	0.187(2)	$-x$	0.2478(6)	1.0
O(3)	18h	0.170(3)	$-x$	0.6975(7)	1.0

[a] $g = 0.833\text{Ba} + 0.167\text{Sr}$.
[b] $g = 0.8\text{Zr} + 0.2\text{Ta}$.

TABLE 5
Positional and Thermal Parameters for $Ba_5SrTa_4ZrO_{21}$

Atom	Position	x/a	y/b	z/c	B_{iso} (Å^2)
BaSr(1)[a]	3a	0	0	0	0.12(9)
BaSr(2)[a]	6c	0	0	0.1540(2)	0.12(9)
BaSr(3)[a]	6c	0	0	0.2356(2)	0.12(9)
BaSr(4)[a]	6c	0	0	0.3857(2)	0.21(9)
TaZr(1)[b]	6c	0	0	0.0723(2)	1.9(1)
TaZr(2)[b]	6c	0	0	0.3102(2)	1.9(1)
TaZr(3)[b]	6c	0	0	0.4582(2)	1.9(1)
O(1)	18h	0.164(4)	$-x$	0.0969(8)	1.0
O(2)	18h	0.169(3)	$-x$	0.4741(7)	1.0
O(3)	18h	0.504(3)	$2x$	0.3838(7)	1.0
O(4)	9e	1/2	0	0	1.0

[a] $g = \frac{5}{7}\text{Ba} + \frac{2}{7}\text{Sr}$.
[b] $g = \frac{2}{3}\text{Ta} + \frac{7}{3}\text{Zr}$.

TABLE 6
Selected Interatomic Distances for $Ba_5SrTa_4ZrO_{21}$ (Å)

BaSr(1)–O(3)	3.03(3) × 6	BaSr(4)–O(3)	2.900(7) × 6
BaSr(1)–O(4)	2.8999(1) × 6	BaSr(4)–O(4)	3.089(7) × 3
BaSr(2)–O(2)	2.52(3) × 3	TaZr(1)–O(1)	2.05(3) × 3
BaSr(2)–O(2)	2.972(8) × 6	TaZr(1)–O(3)	1.94(3) × 3
BaSr(2)–O(1)	3.27(4) × 3	TaZr(2)–O(3)	2.21(3) × 3
BaSr(3)–O(2)	2.70(3) × 3	TaZr(2)–O(4)	2.029(6) × 3
BaSr(3)–O(1)	2.900(7) × 6	TaZr(3)–O(2)	1.88(3) × 3
BaSr(3)–O(3)	2.86(3) × 3	TaZr(3)–O(1)	2.20(3) × 3
BaSr(4)–O(1)	2.79(4) × 3		

This interpretation is supported by computer simulation of the images for different thicknesses and defocus values (Figs. 5a and 5b). The atomic coordinates and occupancies obtained from the X-ray powder refinement were taken as an input. The good agreement between calculated and experimental images confirms the results of the Rietveld refinement of the $Ba_5SrTa_4ZrO_{18}$ and $Ba_5Sr_2Ta_4Zr_2O_{21}$ crystal structures.

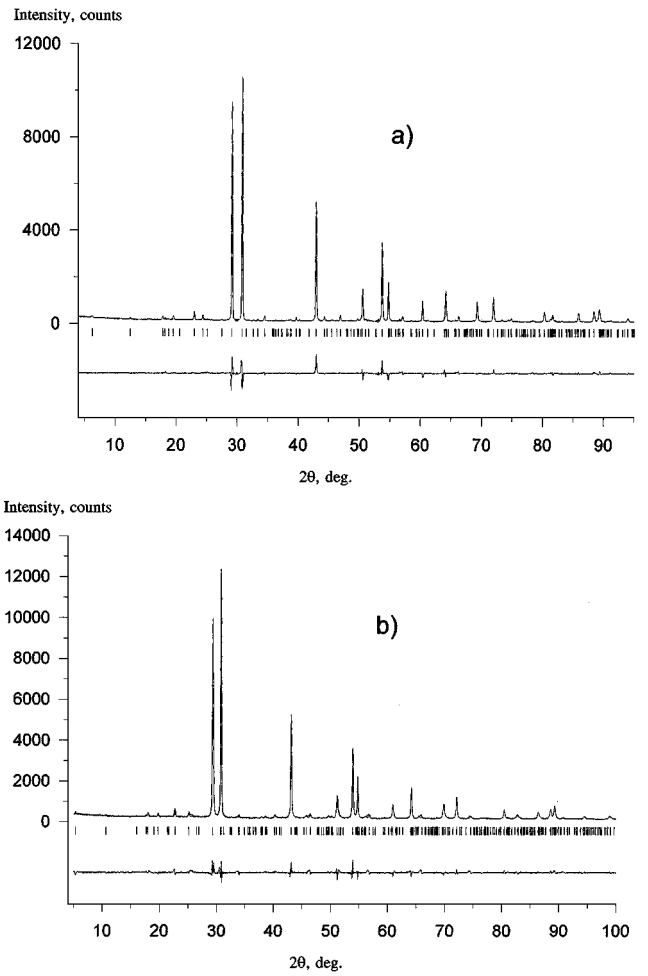

FIG. 1. Experimental, calculated, and difference X-ray patterns for (a) $Ba_5SrTa_4ZrO_{18}$ and (b) $Ba_5Sr_2Ta_4Zr_2O_{21}$.

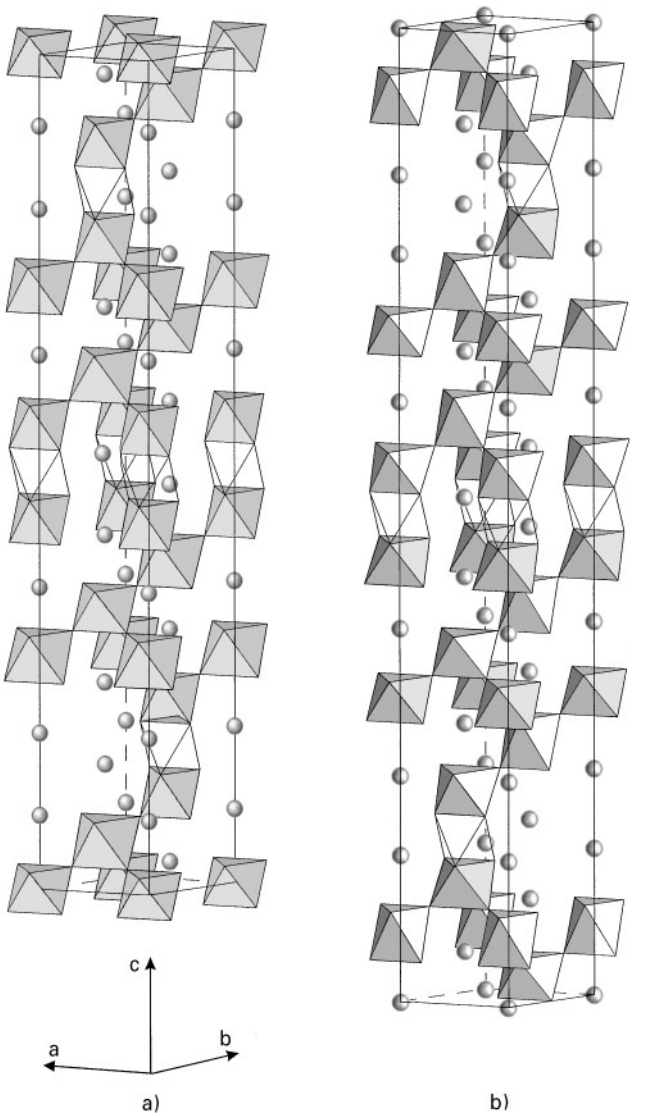

FIG. 2. Crystal structures of (a) $Ba_5SrTa_4ZrO_{18}$ and (b) $Ba_5Sr_2Ta_4Zr_2O_{21}$. The circles represent *A* cations; *B* cations are placed in the shaded octahedra. Vacant octahedra are not shaded.

3.3.2. Defect structure. The high-resolution images of $Ba_5Sr\ Ta_4ZrO_{18}$ and $Ba_5Sr_2Ta_4Zr_2O_{21}$ reveal a variation of the spacing between vacant cation layers in *chhc* triplets. The most frequently observed distances are equal to six $Ba(Sr)O_3$ close-packed layers for $Ba_5SrTa_4ZrO_{18}$ and seven $Ba(Sr)O_3$ layers for $Ba_5Sr_2Ta_4Zr_2O_{21}$. Wider bands, including eight, nine, and more layers, were also found (Figs. 6a and 6b). These wider bands show an image contrast similar to that for the matrix of the perfect structure. Such a violation of the stacking sequence obviously appears to be due to the insertion of additional layers between the *chhc* triplets. The optical diffraction pattern obtained from

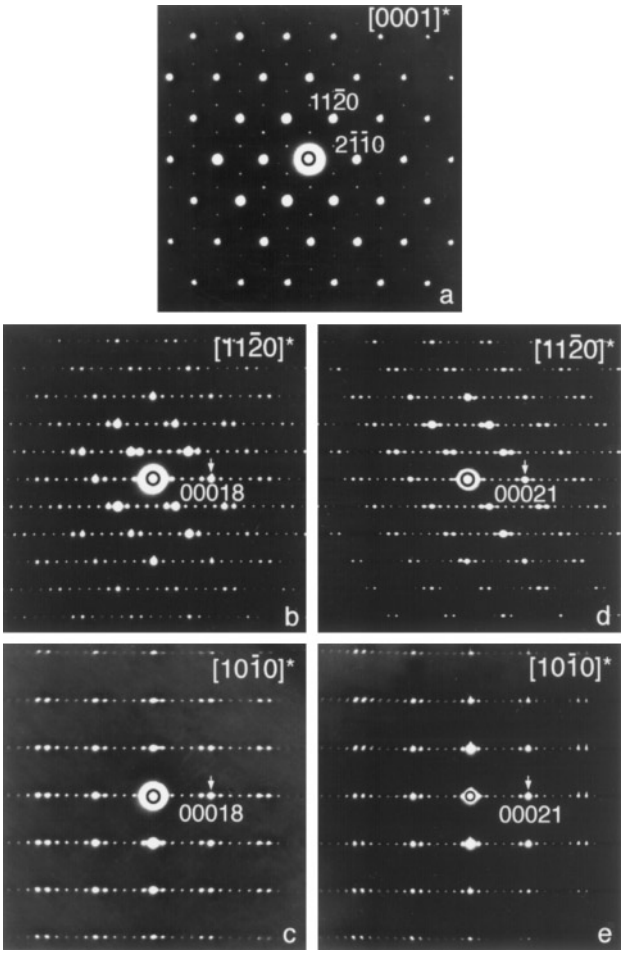

FIG. 3. Electron diffraction patterns along some of the most prominent zone axes for $Ba_5SrTa_4ZrO_{18}$ (a–c) and $Ba_5Sr_2Ta_4Zr_2O_{21}$ (d, e).

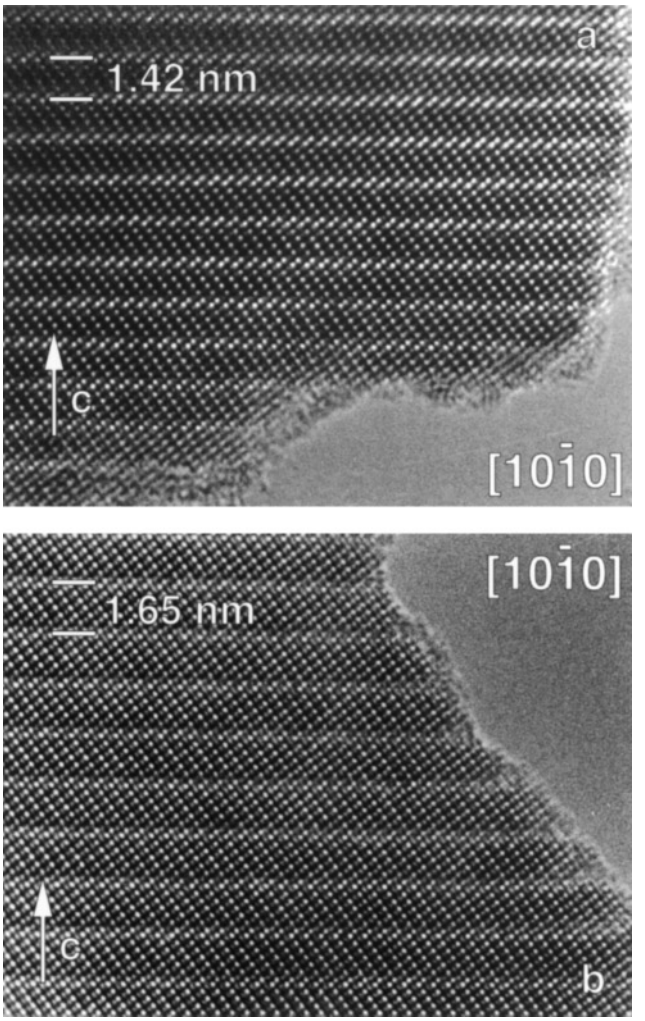

FIG. 4. HREM image along the [10$\bar{1}$0] zone for $Ba_5SrTa_4ZrO_{18}$ (a) and $Ba_5Sr_2Ta_4Zr_2O_{21}$ (b).

the widest observed band (about 20 layers) reveals a spot distribution typical for the cubic perovskite structure. The ratios between interplanar spacings and the relative orientation of the crystallographic planes correspond to the $[110]_c$ zone axis of a primitive cubic lattice. It is reasonable to assume that this structure may be the $(Ba,Sr)ZrO_3$ perovskite forming an epitaxial intergrowth with the initial matrix with common $(111)_c$ and $(0001)_h$ planes, which both are close-packed $Ba(Sr)O_3$ layers.

The high-resolution images of several crystallites in the $Ba_5Sr_2Ta_4Zr_2O_{21}$ sample show the presence of large areas with a well-ordered structure corresponding to an eight-layer stacking sequence *hccccccch*. This structure represents the member $n = 8$ of the $A_nB_{n-1}O_{3n}$ homologous series. Considering this phase to be a result of the intergrowth of $Ba_5Ta_4O_{15}$-type and $SrZrO_3$-type structural blocks, one can deduce the composition as $Ba_5Ta_4O_{15} + 3SrZrO_3$ or $Ba_5Sr_3Ta_4Zr_3O_{24}$. The optical diffraction pattern obtained from the areas of this phase was indexed on a primitive trigonal unit cell with $c/a = 3.26$.

The results of the cell parameter determination by X-ray data (see Table 1) show that there is only a negligible difference between the a parameters for the two successive homologues $Ba_5SrTa_4ZrO_{18}$ and $Ba_5Sr_2Ta_4Zr_2O_{21}$. This observation allows us to propose the same value $a = 5.8$ Å for $Ba_5Sr_3Ta_4Zr_3O_{24}$; the c parameter should then be equal to 18.9 Å. This value can be calculated also using the average thickness of the $Ba(Sr)O_3$ layer determined from structural data for $Ba_5SrTa_4ZrO_{18}$ and $Ba_5Sr_2Ta_4Zr_2O_{21}$ (8×2.36 Å $= 18.88$ Å). Both values, obtained from the high-resolution image or calculated from the layer thickness, are in very good agreement. The known cell dimensions and the stacking sequence give us the possibility to determine an approximate structure model of $Ba_5Sr_3Ta_4Zr_3O_{24}$. The most symmetrical space group compatible with the observed stacking sequence is $P\bar{3}m1$. The atomic coordinates for A cations, B cations, and oxygen atoms were chosen according to the undistorted *hccccccch* close packing.

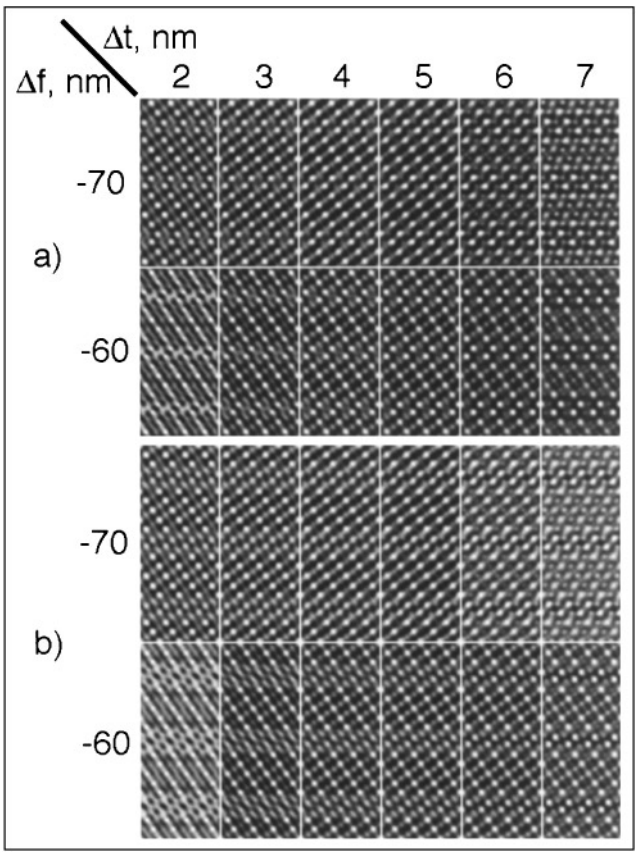

FIG. 5. Matrix of calculated high-resolution images along the [10$\bar{1}$0] zone for $Ba_5SrTa_4ZrO_{18}$ (a) and $Ba_5Sr_2Ta_4Zr_2O_{21}$ (b) for different thicknesses and defocus values.

The cation vacancies were placed in the middle octahedron of the *chhc* lamellae. The simulated images were computed assuming a full random occupation of the *A* positions by Ba and Sr and the *B* positions by Ta and Zr. The good agreement between the experimental image and calculated one (Fig. 7) confirms the model proposed for the $Ba_5Sr_3Ta_4Zr_3O_{24}$ crystal structure.

Secondary defects, which are relevant for the formation mechanism of equispaced arrays of planar faults, are visible in Fig. 8. They consist of steps in the fault plane. On one side of the step, the lamellae above and below the stepped interface contain respectively six and seven years, whereas they contain seven and six layers on the other side. A sideways shift of the step requires only short-range diffusion and changes the lamellae width by one layer; it thus allows a rearrangement of the faults into an equally spaced array, minimizing in this way the free energy associated with the faults. A similar mechanism was suggested earlier in relation with the observations on the La–Ti–O system (1).

The high-resolution image represented in Fig. 9a shows the presence of a 60° rotation microtwin. The slab indicated by a white arrow is an isolated [01$\bar{1}$0]-oriented lamella in a [10$\bar{1}$0]-oriented matrix of the $Ba_5Sr_2Ta_4Zr_2O_{21}$ compound. The experimental image can be compared with the schematic model in Fig. 10. The rotated lamella (marked by a bracket) is shifted by (1/3,2/3,0) to achieve matching between adjacent [10$\bar{1}$0]-oriented lamellae; the corresponding glide planes are marked by arrows. The pairs of FSO appear due to the shift of the twin lamella. They should be randomly occupied by Ta, Zr, and cation vacancies, thus decreasing the electrostatic repulsion between *B* cations, probably in a manner similar to that found in the $Ba_8Ta_4Ti_3O_{24}$ oxide (12).

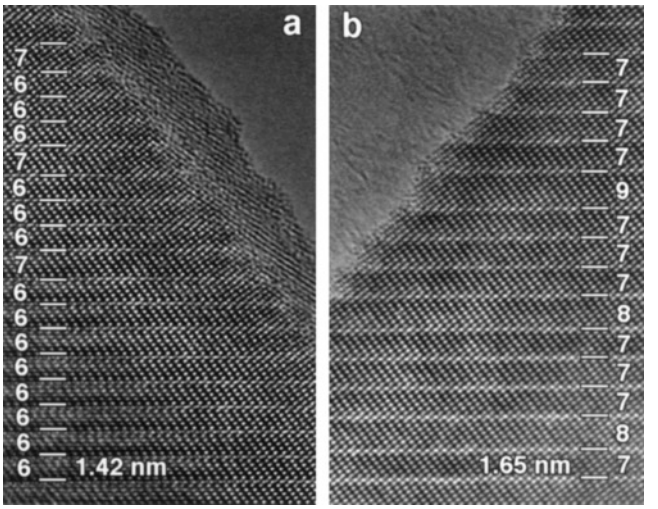

FIG. 6. HREM images along the [10$\bar{1}$0] zone showing a violation of stacking sequence due to the insertion of additional close-packed layers for $Ba_5SrTa_4ZrO_{18}$ (a) and $Ba_5Sr_2Ta_4Zr_2O_{21}$ (b).

A more drastically faulted area is shown in Fig. 9b. A 6-layered twin lamella, passing through the 21-layered matrix, ends within a matrix of the 18-layered compound.

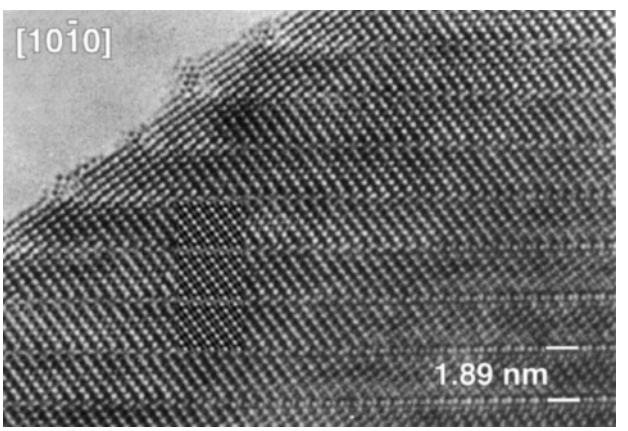

FIG. 7. HREM image along the [10$\bar{1}$0] zone for $Ba_5Sr_3Ta_4Zr_3O_{24}$. The calculated image (− 600-Å defocus, 30-Å thickness) is shown as an inset.

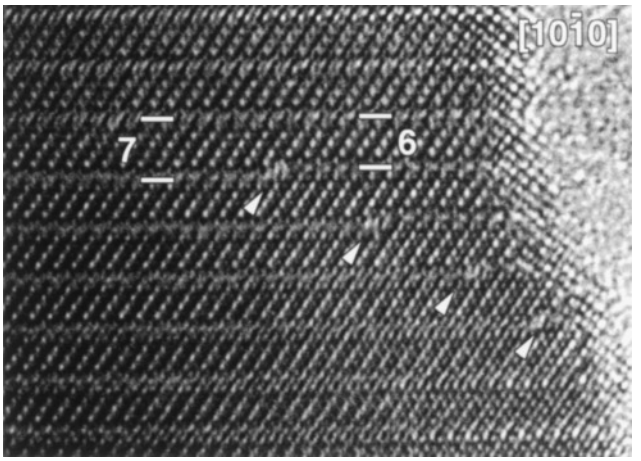

FIG. 8. HREM image for $Ba_5SrTa_4ZrO_{18}$ representing an equispaced array of stacking faults. The stepped interfaces are marked by arrows.

This disturbance is accommodated by the formation of an ending fault plane in the crystal part facing the end of the twin lamellae. Also a number of "steps" are formed in the adjacent fault planes. A real-space Burgers circuit around the defect area, passing exclusively in perfect areas, exhibits a "closure failure". The total "Burgers vector" has a component along [0001] with a length equal to three layers. However, an unambiguous model for this dislocation structure cannot be proposed due to a lack of adequate image resolution in the faulted area.

4. DISCUSSION

The $Ba_5SrTa_4ZrO_{18}$ and $Ba_5Sr_2Ta_4Zr_2O_{21}$ crystal structures consist of *chhc* lamellae separated by two and three close-packed layers, respectively. The Rietveld refinement revealed that the middle octahedron of the *chhc* lamellae remains vacant for both $Ba_5SrTa_4ZrO_{18}$ and $Ba_5Sr_2Ta_4Zr_2O_{21}$ compounds. Indeed, these compounds belong to the $A_nB_{n-1}O_{3n}$ homologous series of hexagonal perovskites. Their crystal structures can be formally described as the result of an ordered alternation of the $Ba_5Ta_4O_{15}$-type and $MZrO_3$-type (M = Ba, Sr) structural blocks along the c axis. Ba(Sr)ZrO_3 has an ideal cubic perovskite structure, which is based on a (*ccc*) close packing along the [111] direction of a cubic cell. This fact allows us to consider these structures as intergrowth structures (Fig. 11).

The ratio between structural blocks of $Ba_5Ta_4O_{15}$: $MZrO_3 = 1:1$ and the presence of *chhc* lamellae with a vacant middle octahedron define the minimal number of close-packed layers in the structure of the $Ba_5MTa_4ZrO_{18}$ compound. The 6-layer packing does not contain the *chhc* lamellae, whereas the 12-layer packing with symmetry C_{6v}^4 contains both *chhc* and *chc* (two FSO) lamellae. If

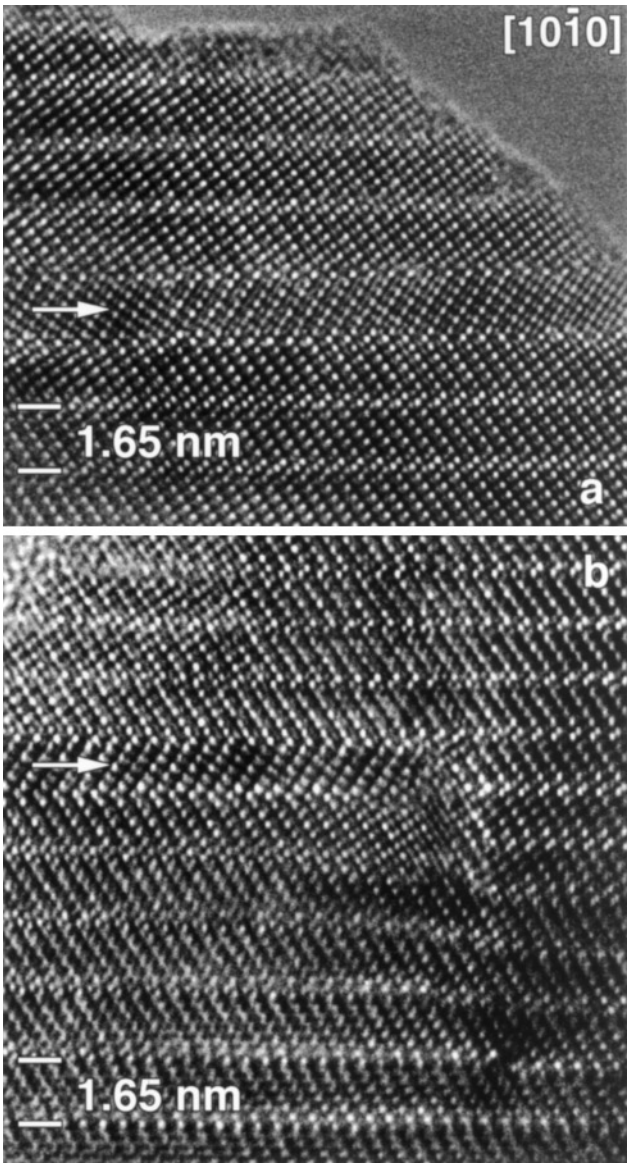

FIG. 9. An area of the 21-layered close-packed structure containing a microtwin lamella. (b) The interface between the 21-layered matrix with a twin lamella and the 18-layered matrix. The twin lamella is indicated by an arrow.

cation vacancies are located in the *chhc* lamellae, two FSO of the *chc* fragment should be completely filled by *B* cations. The placement of highly charged cations with such a short separation (equal to an average distance of 2.36 Å between close-packed layers) should destabilize this structure due to a strong electrostatic repulsion. This consideration allows us to deduce the minimum number of close-packed layers to be equal to 18.

Earlier we reported an investigation of the related $Ba_5Ta_4O_{15}$–$BaTiO_3$ system (12), where two compounds, $Ba_8Ta_4Ti_3O_{24}$ and $Ba_{10}Ta_{7.04}Ti_{1.2}O_{30}$, were found. Both

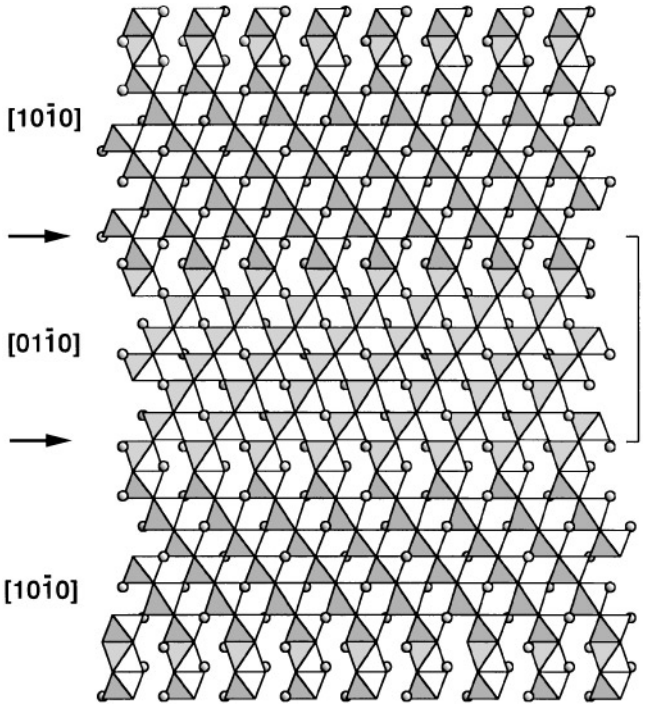

FIG. 10. A structural model of the microtwin shown in Fig. 9a. Shaded octahedra contain *B* cations or cation vacancies; *A* cations are shown as circles.

compounds form solid solutions with wide homogeneity ranges—$Ba_8Ta_{4-0.8x}Ti_{3-x}O_{24}$ $(0 \le x \le 0.8)$ and $Ba_{10}Ta_{8-0.8x}Ti_xO_{30}$ $(0.6 \le x \le 1.2)$—and their structures are based on 8H $(cchc)_2$ and 10H $(cchcc)_2$ close packings, respectively. It is easy to see that the $Ba_7Ta_4Ti_2O_{21}$ (or $Ba_8Ta_{4.57}Ti_{2.28}O_{24}$) composition is inside the homogeneity range of the $Ba_8Ta_{4-0.8x}Ti_{3-x}O_{24}$ solid solution. Moreover, the $Ba_8Ta_4Ti_3O_{24}$ composition directly corresponds to the $A_nB_{n-1}O_{3n}$ homologue with $n = 8$, which was found in the $Ba_5Ta_4O_{15}$–$SrZrO_3$ system ($Ba_5Sr_3Ta_4Zr_3O_{24}$). However, in spite of the close behavior of Ti^{4+} and Zr^{4+} cations, the crystal structures of $Ba_7Ta_4Ti_2O_{21}$ and $Ba_7Ta_4Zr_2O_{21}$ as well as $Ba_8Ta_4Ti_3O_{24}$ and $Ba_5Sr_3Ta_4Zr_3O_{24}$ differ significantly. The main feature of the structures in the $Ba_5Ta_4O_{15}$–$BaTiO_3$ system is the presence of pairs of FSO randomly occupied by Ta atoms, Ti atoms, and cation vacancies. Since these structures do not contain groups of three FSO and since the placement of *B* cations and vacancies is random, they cannot be considered as members of the $A_nB_{n-1}O_{3n}$ homologous series. Moreover, Ti-containing $Ba_nB_{n-1}O_{3n}$ homologues were not found at any $Ba_5Ta_4O_{15}$: $BaTiO_3$ ratio. Possibly, the origin of the different behaviors of the $Ba_5Ta_4O_{15}$–$BaTiO_3$ and $Ba_5Ta_4O_{15}$–$Ba(Sr)ZrO_3$ systems could be connected with the smaller ionic radius of Ti^{4+} (0.605 Å) in comparison with that of Zr^{4+} (0.72 Å) (13). The smaller size of the Ti^{4+} cation prevents matching between the parent $Ba_5Ta_4O_{15}$ and $BaTiO_3$ blocks and intergrowth structures are not formed. The Ti-containing $A_nB_{n-1}O_{3n}$ homologues with $n = 4$–6 were obtained when large Ba^{2+} ($r = 1.60$ Å) cations were replaced by La^{3+} ($r = 1.32$ Å) and Ca^{2+} ($r = 1.35$ Å) (1, 7–10).

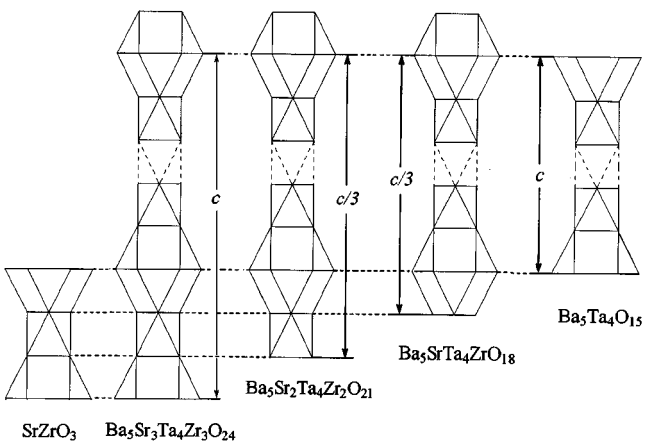

FIG. 11. Formation of $Ba_5SrTa_4ZrO_{18}$, $Ba_5Sr_2Ta_4Zr_2O_{21}$, and $Ba_5Sr_3Ta_4Zr_3O_{24}$ structures as a result of the intergrowth of $Ba_5Ta_4O_{15}$ and $SrZrO_3$ blocks.

ACKNOWLEDGMENTS

This work was supported by the Russian Science Foundation (Grant 97-03-33432a). A.M.A. and O.I.L. are grateful to DWTC and FWO (Belgium), respectively, for financial support during their stay at the University of Antwerp. This work has been performed within the framework of IUAP 4/10.

REFERENCES

1. G. Van Tendeloo, S. Amelinckx, B. Darriet, R. Bontchev, J. Darriet, and F. Weill, *J. Solid State Chem.* **108,** 314 (1994).
2. C. Calvo, H. N. Ng, and B. L. Chamberland, *Inorg. Chem.* **17,** 699 (1978).
3. J. Shannon and L. Katz, *Acta Crystallogr., Sect. B* **26,** 102 (1970).
4. H.-J. Roter and S. Kemmler-Sack, *Z. Anorg. Allg. Chem.* **465,** 179 (1980).
5. W. Wischert, H.-J. Schittenhelm, and S. Kemmler-Sack, *Z. Anorg. Allg. Chem.* **448,** 119 (1979).
6. B. Mîssner and S. Kemmler-Sack, *J. Less-Common Met.* **120,** 287 (1986).
7. N. Fedorov, O. Melnikova, V. Saltykova and M. Chistjakova, *Russ. J. Inorg. Chem.* **25,** 1166 (1979).
8. M. German and L. Kovba, *Russ. J. Inorg. Chem.* **28,** 2377 (1983).
9. M. German and L. Kovba, *Russ. J. Inorg. Chem.* **30,** 317 (1985).
10. R. Bontchev, B. Darriet, J. Darriet, F. Weill, G. Van Tendeloo, and S. Amelinckx, *Eur. J. Solid State Inorg. Chem.* **30,** 521 (1993).
11. F. Izumi, *in* "The Rietveld Method" (R. A. Young, Ed.), Chap. 13. Oxford Univ. Press, Oxford, 1993.
12. R. Shpanchenko, L. Nistor, G. Van Tendeloo, J. Van Landuyt, S. Amelinckx, A. Abakumov, E. Antipov, and L. Kovba, *J. Solid State Chem.* **114,** 560 (1995).
13. R. D. Shannon and C. T. Prewitt, *Acta Crystallogr., Sect. B* **25,** 925 (1969).